RESEARCH ARTICLE SUMMARY

HYBRID PEROVSKITES

Atomic-scale microstructure of metal halide perovskite

Mathias Uller Rothmann, Judy S. Kim, Juliane Borchert, Kilian B. Lohmann, Colum M. O'Leary, Alex A. Sheader, Laura Clark, Henry J. Snaith, Michael B. Johnston, Peter D. Nellist*, Laura M. Herz*

INTRODUCTION: Hybrid metal halide perovskites are highly favorable materials for efficient photovoltaic and optoelectronic applications. The mechanisms behind their impressive performance have yet to be fully understood, but they likely depend on atomic-level properties that may be unique to these perovskites. Atomic-resolution transmission electron microscopy is well suited to provide new insights but is challenging because of the highly beam-sensitive nature of hybrid perovskites.

RATIONALE: We used low-dose scanning transmission electron microscopy (STEM) imaging to determine the microstructure of thin hybrid perovskite films. Thermally evaporated thin films of formamidinium and methylammonium lead triiodide ($FAPbI_3$ and $MAPbI_3$, respectively) were examined on ultrathin carbon-coated copper TEM grids to reveal the nature of boundaries, defects, and decomposition pathways.

RESULTS: Using low-dose low-angle annular dark field (LAADF) STEM imaging, we obtained atomic-resolution micrographs of $FAPbI_3$ films in the cubic phase. We found that prolonged electron irradiation leads to a loss of FA^+ ions, which initially causes the perovskite structure to change to a partially FA^+-depleted but ordered perovskite lattice, apparent as light-and-dark checkered patterns in STEM images. Further electron beam exposure leads to the expected deterioration to PbI_2 as the final decomposition product. We propose that the observed intermediate checkered pattern is triggered by an initially random, beam-induced loss of FA^+, followed by subsequent reordering of FA^+ ions. The discovery of this intermediate structure explains why the perovskite structure can sustain significant deviations from stoichiometry and recovers remarkably well from damage.

We further revealed the atomic arrangement at interfaces within the hybrid perovskite films. We found that PbI_2 precursor remnants commonly encountered in hybrid perovskite films readily and seamlessly intergrow with the $FAPbI_3$ and $MAPbI_3$ lattice and can distort from their bulk hexagonal structure to form a surprisingly coherent transition boundary, exhibiting low lattice misfit and strain. We observed PbI_2 domains that nearly perfectly follow the surrounding perovskite structure and orientation, which suggests that PbI_2 may seed perovskite growth. These observations help to explain why the presence of excess PbI_2 tends not to impede solar cell performance.

Images of $FAPbI_3$ grain boundaries further revealed that the long-range perovskite structure is preserved up to the grain boundaries, where sharp interfaces are generally present, without any obvious preferred orientation. Near-120° triple boundaries are most commonly observed at the intersection of three grains, which we generally found to be crystallographically continuous and associated with minimal lattice distortion.

Finally, we identified the nature of defects, dislocations, and stacking faults in the $FAPbI_3$ lattice. We discovered dislocations that are dissociated in a direction perpendicular to their glide plane (climb-dissociated), aligned point defects in the form of vacancies on the Pb-I sublattice, and stacking faults corresponding to a shift of half a unit cell, connecting Pb-I columns with I^- columns rather than with FA^+ columns.

CONCLUSION: Our findings provide an atomic-level understanding of the technologically important class of hybrid lead halide perovskites, revealing several mechanisms that underpin their remarkable performance. The highly adaptive nature of the perovskite structure upon organic cation loss yields exceptional regenerative properties of partly degraded material. The observation of coherent perovskite interfaces with PbI_2 explains the barely diminished optoelectronic performance upon such precursor inclusions, while sharp interfaces between perovskite grains grant a benign nature. Such atomically localized information enables the targeted design of methods to eliminate defects and optimize interfaces in these materials. ■

The list of author affiliations is available in the full article online.
*Corresponding author. Email: laura.herz@physics.ox.ac.uk (L.M.H.); peter.nellist@materials.ox.ac.uk (P.D.N.)
Cite this article as M. U. Rothmann *et al.*, *Science* **370**, eabb5940 (2020). DOI: 10.1126/science.abb5940

READ THE FULL ARTICLE AT
https://doi.org/10.1126/science.abb5940

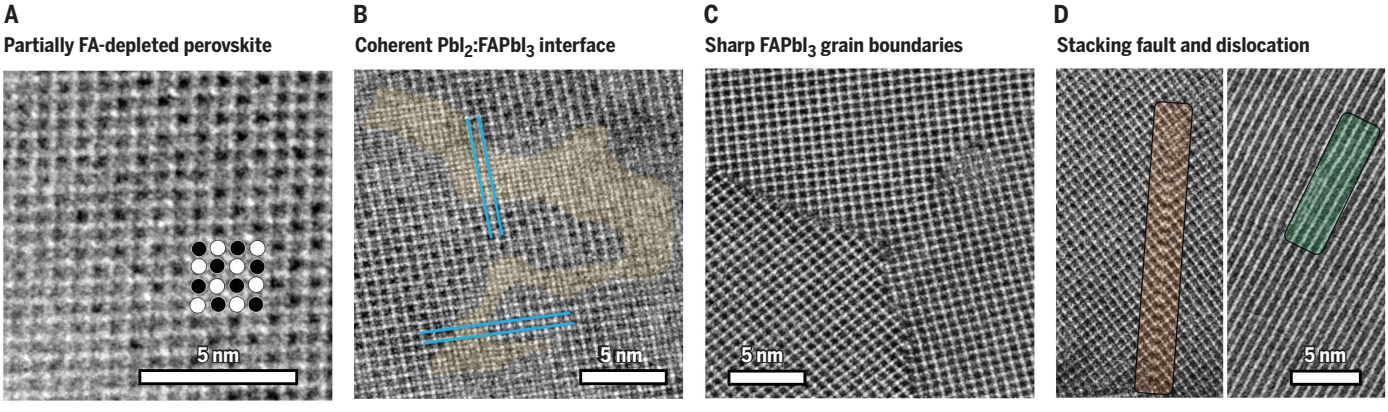

Atomic-resolution STEM images of $FAPbI_3$. (**A**) Checkered intensity pattern formed upon electron beam exposure with ~200 e $Å^{-2}$. (**B**) Native intergrowth between PbI_2 (shaded yellow) and $FAPbI_3$ within the vapor-deposited film. (**C**) Abrupt grain boundaries meeting at a near-120° triple junction, showing no amorphous or intergranular phase. (**D**) Intrinsic stacking fault (orange rectangle, left) and climb-dissociated dislocation (green rectangle, right). Scale bars, 5 nm.

RESEARCH ARTICLE

HYBRID PEROVSKITES

Atomic-scale microstructure of metal halide perovskite

Mathias Uller Rothmann[1], Judy S. Kim[2,3,4], Juliane Borchert[1], Kilian B. Lohmann[1], Colum M. O'Leary[2], Alex A. Sheader[2], Laura Clark[2], Henry J. Snaith[1], Michael B. Johnston[1], Peter D. Nellist[2]*, Laura M. Herz[1]*

Hybrid organic-inorganic perovskites have high potential as materials for solar energy applications, but their microscopic properties are still not well understood. Atomic-resolution scanning transmission electron microscopy has provided invaluable insights for many crystalline solar cell materials, and we used this method to successfully image formamidinium lead triiodide [$CH(NH_2)_2PbI_3$] thin films with a low dose of electron irradiation. Such images reveal a highly ordered atomic arrangement of sharp grain boundaries and coherent perovskite/PbI_2 interfaces, with a striking absence of long-range disorder in the crystal. We found that beam-induced degradation of the perovskite leads to an initial loss of formamidinium [$CH(NH_2)_2^+$] ions, leaving behind a partially unoccupied perovskite lattice, which explains the unusual regenerative properties of these materials. We further observed aligned point defects and climb-dissociated dislocations. Our findings thus provide an atomic-level understanding of technologically important lead halide perovskites.

Many of the advances in the performance of hybrid metal halide perovskite (MHP) solar cells have resulted from improvements in device architecture and material composition studied on a mesoscopic to macroscopic scale (*1*–*7*), and changes in material properties have usually been inferred from relatively "large area" probes (*8*–*11*). Although these probes can resolve properties on the scale of a few hundred nanometers to a few millimeters, the mechanisms behind the impressive performance of hybrid perovskites have yet to be fully understood. However, the atomic-level nature of their properties can be inferred from the gradual rather than abrupt decrease in photovoltaic performance of MHPs over time (*12*), their ability to readily regenerate when exposed to gaseous iodo-organic precursors (*13*), and the counterintuitively beneficial effects of adding a small excess of PbI_2 [2% (*14*, *15*) to 7.5% (*16*)] to the MHP precursor solution. Similarly, substantial efforts have been made to describe the properties of grain boundaries in MHP thin films by means of light and scanning probes (*17*–*19*), with highly inconsistent results (*11*, *17*). Recent work has shown that a smaller spread of grain boundary orientations increases the photoluminescence intensity locally (*20*), but the exact atomic nature of grain boundaries has still not been described. Even the crystal phase of the technologically important $CH(NH_2)_2PbI_3$ (formamidinium lead triiodide, $FAPbI_3$) MHP is still uncertain (*21*). Therefore, truly atomic-resolution imaging of MHPs has great potential to provide urgently needed understanding for a plethora of puzzling observations already established for perovskite devices, which in turn would lead to a further increase in their efficiency. In addition, grain boundaries have been postulated to have a substantial impact on the long-term stability of MHPs (*22*, *23*), yet their exact nature is still mostly unknown.

Atomic-resolution transmission electron microscopy (TEM) may be of use in clarifying some of these aspects of MHPs, as it has for other crystalline solar cell materials (*24*, *25*), but the highly beam-sensitive nature of hybrid perovskites makes high-resolution electron microscopy extremely challenging. Although fully inorganic photoactive perovskites have been successfully imaged (*26*), the few studies observing the pristine hybrid perovskite phase are based on nanostructures (*27*, *28*), and no studies of pristine, native hybrid perovskite thin films have been published to date. Unstable under electron beams, MHPs rapidly change into a more stable PbI_2 phase under even mild electron irradiation (*29*, *30*), which has resulted in striking differences in the crystallography reported by electron microscope and x-ray studies (*11*).

Imaging the perovskite structure

We used low-dose scanning transmission electron microscopy (STEM) to obtain images of pristine $FAPbI_3$, because it has been shown for other materials to produce less damage with the same total electron fluence (dose) (*31*). To resolve both "near-stoichiometric" polycrystalline $FAPbI_3$ films and those formed with substantial excess PbI_2 precursor ("PbI_2-rich"), we prepared two different types of thermally evaporated materials on ultrathin carbon-coated copper TEM grids: thinner 30-nm $FAPbI_3$ films close to stoichiometry [FA:Pb:I ratios close to 1:1:3, containing a small excess of PbI_2 (as used to optimize for solar cell applications) (*32*)] and thicker 90-nm films containing substantial excess PbI_2. To examine whether similar atomic-scale microstructures were also observable for methylammonium lead triiodide ($MAPbI_3$), we also deposited 30-nm $MAPbI_3$ films containing substantial excess PbI_2. Full details of the sample preparation procedures and characterization are provided in the supplementary materials and fig. S1. We have reported thin films of $FAPbI_3$ and $MAPbI_3$ deposited by us from such dual-source vapor-deposition protocols to achieve photovoltaic power conversion efficiencies of 14.2 to 18.2% when incorporated into suitable device architectures (*32*, *33*). STEM samples were annealed according to protocols previously developed to optimize photovoltaic performance.

In Fig. 1, we show a low-angle annular dark field (LAADF, inner radius of 33 mrad; see materials and methods for full low-dose image acquisition conditions) STEM micrograph of a 90-nm $FAPbI_3$ film containing excess PbI_2. LAADF STEM is similar to high-angle annular dark field (HAADF) STEM in that it detects scattered electrons, making it sensitive to atomic number (Z) variations, but has the advantage of collecting a higher fraction of the scattered electrons, leading to a higher atomic detection efficiency. In addition, LAADF STEM allows efficient imaging of lower-Z elements, which scatter at lower angles (*34*). To improve the contrast of this image of a pristine crystal, we applied a Bragg filter, as described in detail in materials and methods and in fig. S2.

The lower-magnification image in Fig. 1A reveals an atomic lattice pattern consistent with a cubic structure observed along the ⟨001⟩ orientation. The magnified image in Fig. 1B clearly shows the atomic-level crystal structure corresponding to the cubic structure of room-temperature $FAPbI_3$, displayed schematically in Fig. 1C (*21*). We note that the preferred alignment of growth along the [100] axis ("face-up") is generally observed by us in these dual-source vapor-deposited films and is common for lead halide perovskite deposited across a variety of alternative processing techniques (*35*). We also note that an important advantage of LAADF imaging in this case is that, similar to HAADF imaging, the column intensities retain a monotonic dependence on atomic number. For completeness, a comparison with a HAADF image, acquired as described in materials and methods, is shown in fig. S3.

[1]Department of Physics, Clarendon Laboratory, University of Oxford, Oxford OX1 3PU, UK. [2]Department of Materials, University of Oxford, Oxford OX1 3PH, UK. [3]ePSIC, Diamond Light Source, Harwell, Didcot OX11 0DE, UK. [4]Rosalind Franklin Institute, Harwell, Didcot OX11 0QS, UK.
*Corresponding author. Email: laura.herz@physics.ox.ac.uk (L.M.H.); peter.nellist@materials.ox.ac.uk (P.D.N.)

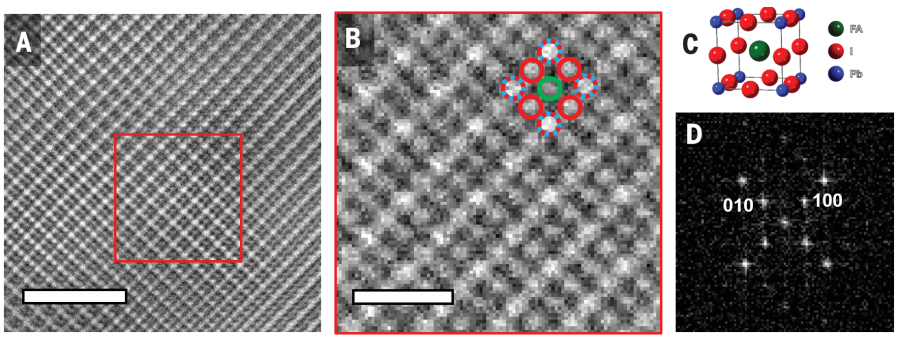

Fig. 1. Atomic-resolution imaging of the metal halide perovskite structure. (**A**) Bragg-filtered atomic-resolution LAADF STEM micrograph of a pristine 90-nm-thick, ⟨001⟩-oriented $FAPbI_3$ film fabricated with excess PbI_2. A distinct pattern in the contrast of the individual atomic columns is clearly visible. (**B**) Magnification of the area within the red square in (A). Here, the variations in composition appear as differences in contrast; the dashed blue and red circles show the Pb/I columns, the red circles show the pure I columns, and the green circle shows the FA^+ columns. (**C**) The atomic unit cell represented by the circles in (B). (**D**) The Fourier transformation (FT) confirms the presence of the {010} and {100} planes, which are often missing from atomic-resolution studies of beam-damaged $FAPbI_3$. Scale bars, 5 nm (A), 1 nm (B). The total dose used for image acquisition in (A) and (B) is ~100 e $Å^{-2}$. See fig. S2 for a comparison of the full image for raw (unfiltered), Butterworth-filtered, and Bragg-filtered data.

Three levels of intensity are observable in the LAADF images. The brightest corresponds to the corners of the cubic unit cell (dashed blue and red circles in Fig. 1B), containing alternating lead and iodine, which are both strongly scattering elements. The second brightest intensity corresponds to the edges of the unit cell containing only iodine, illustrated by the red circles in Fig. 1B. In the z viewing direction, the corners make up a total of one lead atom and one iodine per unit cell, whereas the edge position only contains one iodine, resulting in less scattering and a less bright image intensity. The central, lowest-intensity position corresponds to the FA^+ ions, which scatter the least because of their organic nature and singular presence in the center of the unit cell (*34*). Intensity line profiles and a multislice simulation verifying the differences in contrast are provided in fig. S4.

To support structure identification, we performed a Fourier transformation (FT; Fig. 1D) on the area marked in Fig. 1A, which clearly identifies the presence of the (100) and (010) planes along with the (200) and (020) planes. Of the three proposed room-temperature crystal phases of $FAPbI_3$ [cubic, trigonal, and hexagonal (*21*)], the spots corresponding to the (100) and (010) planes are unique to the cubic perovskite structure and cannot correspond to either of the other two. This strongly indicates that the room-temperature phase of $FAPbI_3$ is cubic in the $Pm\bar{3}m$ space group.

We note that the (100) and (010) FT spots evident in Fig. 1D have been absent in previous atomic-resolution STEM studies of both $FAPbI_3$ and $MAPbI_3$, with only the supposed (200) and (020) or other higher-index spots still visible (*36*–*39*). Broad-beam diffraction studies carried out on $MAPbI_3$ have explained this apparent absence of lower-order diffraction signatures as the result of structural damage caused by high electron irradiation dosage (*29*, *30*). Thus, the spots attributed to the second-order diffraction off the perovskite lattice may instead derive from the PbI_2 formed as a decomposition product under intense electron irradiation (*40*, *41*).

Electron-induced decomposition

Using a suitably chosen irradiation dosage, we were able to observe the gradual decomposition of $FAPbI_3$ with electron beam exposure. Figure 2A shows a lower-magnification Butterworth-filtered LAADF image of a pristine grain boundary in a 30-nm-thick $FAPbI_3$ film close to stoichiometry on a carbon-coated TEM grid after a single scan of the electron beam, with a total dose of ~66 e $Å^{-2}$. The subsequent scans were also recorded (Fig. 2, B to D). After three scans (~200 e $Å^{-2}$), the contrast within the perovskite structure has visibly changed, and after nine scans (~600 e $Å^{-2}$), the perovskite structure is completely depleted and replaced by a crystal structure with uniform column intensities (Fig. 2C). Further extensive exposure (~1333 e $Å^{-2}$) slightly alters this phase so that it is very similar to 2H-hexagonal PbI_2 (Fig. 2D). This final structure is highly stable, does not change substantially after further exposure, and corresponds well to the PbI_2 phase observed by diffraction in broad-beam TEM studies (*29*). A full crystallographic determination of the phase seen in Fig. 2C is beyond the scope of this study, but fig. S10 shows how a small distortion of hexagonal PbI_2 can form a structure that projects as a square lattice and forms a coherent epitaxial interface with $FAPbI_3$ as observed in the image data. The FTs in Fig. 2, E to H, show the degradation process on a crystallographic level: For the pristine perovskite, diffraction spots corresponding to the {100} plane family are initially clearly visible (Fig. 2E). Additional spots appear after brief exposure (Fig. 2F, orange circles), likely corresponding to the ordered loss of formamidinium ions discussed below. Continued exposure fully destroys the perovskite structure, transforming it into electron irradiation–stable PbI_2 concomitant with the disappearance of the {100} plane family of the original perovskite (Fig. 2G) and finally into a structure similar to that of 2H-hexagonal PbI_2 (Fig. 2H).

Nanoscopic properties of metal halide perovskites

The implementation of a low electron dose, <200 e $Å^{-2}$, inevitably results in a low signal-to-noise ratio when images are recorded. We find that combining low-dose LAADF imaging with simple Butterworth and Bragg filters allows us to investigate pristine and slightly damaged $FAPbI_3$ thin films with atomic resolution, observing phenomena invisible to other techniques. The details of each filtering technique are provided in materials and methods and in fig. S5. Our findings are based on hundreds of STEM images taken across seven or eight thin-film samples prepared for each stoichiometry; the images we present were carefully chosen to be representative of each material's microstructural features.

In Fig. 3, A to C, we show LAADF images of polycrystalline perovskite films fabricated with excess PbI_2. We observe a surprisingly coherent transition boundary between remnant precursor PbI_2 (highlighted in light orange) and the $FAPbI_3$ grains, with undetectable lattice misfit. In addition, a light and dark checkered pattern becomes clearly visible in images of $FAPbI_3$ after mild radiation damage, as highlighted schematically in the lower right of Fig. 3A through white and black circles and seen surrounding the PbI_2 region in Fig. 3D. We propose that the observed checkered pattern in the central position of the $FAPbI_3$ unit cell is triggered by an initially random, beam-induced loss of FA^+, likely due to dissociation of the FA^+ by radiolysis (*42*, *43*), potentially complemented by loss of I^- through knock-on (displacement) effects (*41*). We postulate that the remaining FA^+ ions then migrate to form an ordered structure with an associated energy reduction that helps to stabilize the FA^+-deficient structure. Such migration of FA^+ ions within the perovskite structure after electron irradiation then results in the observed checkered pattern as an intermediate equilibrium (*29*). A degradation mechanism assuming solely the ordered loss of I^- was previously proposed on the basis of analysis of diffraction

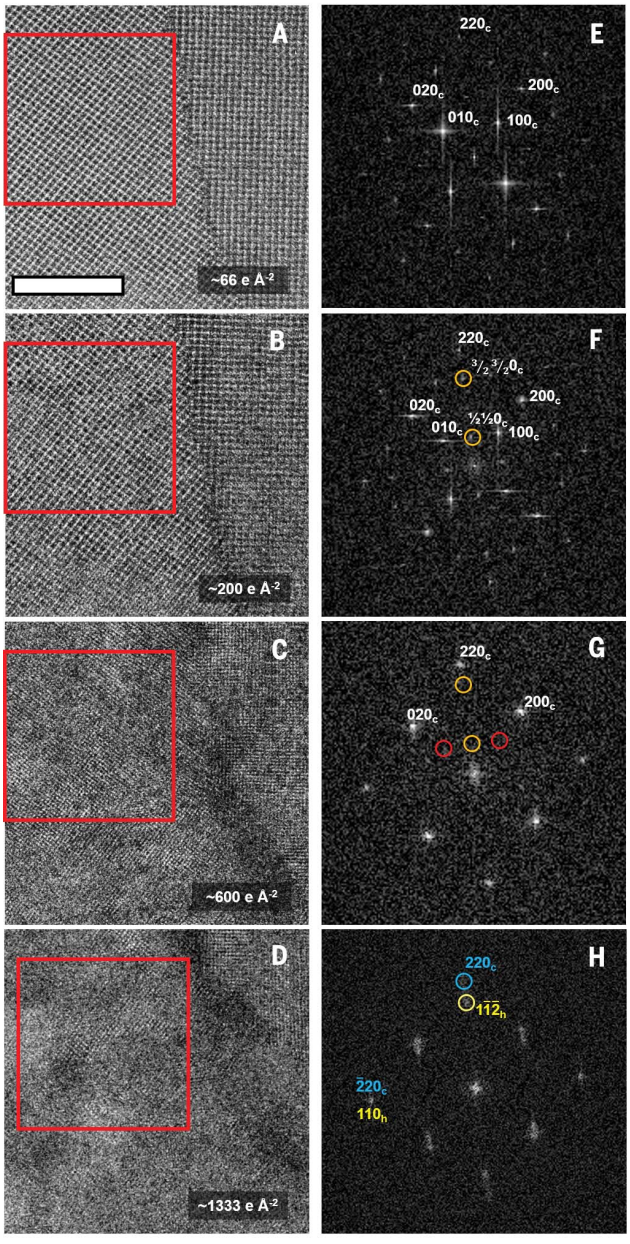

Fig. 2. Damage mechanism of $FAPbI_3$ under a scanning electron beam observed in a 30-nm-thick film prepared near the correct stoichiometry. (**A**) The first scan (~66 e $Å^{-2}$) shows the pristine perovskite structure and a grain boundary. (**B**) After three scans (~200 e $Å^{-2}$), changes in the crystal structure are apparent in the LAADF image but the grain boundary is still distinguishable. (**C**) After nine scans (~600 e $Å^{-2}$), the perovskite structure has fully disappeared and a new crystalline phase has replaced it. Different crystal orientations are visible, but there is no clear grain boundary. (**D**) After 20 scans (~1333 e $Å^{-2}$), the angles of the crystal planes change slightly, indicating the complete transformation into 2H-PbI_2. (**E** to **H**) The Fourier transformations corresponding to the areas in the red squares in (A) to (D), respectively, confirm the dynamic radiation-induced transformation. Initially, the FT in (E) reveals a pristine cubic structure, but additional spots appear after brief exposure, circled in orange in (F). After further exposure, the additional spots disappear again, along with the {100} spots, whose expected location is marked by red circles in (G). Finally, after extended exposure, the FT contains two sets of spots: one set that can be indexed with the degraded cubic phase and another corresponding to the hexagonal PbI_2 phase, marked with a blue and a yellow circle in (H), respectively. The $\bar{2}20_c$ (2.2493 Å) and 110_h (2.2775 Å) spots overlap, indicating an intergrowth of the two phases. Indices marked with a subscript "c" are from the epitaxial $FAPbI_3$ phase; those marked with a subscript "h" are from the hexagonal PbI_2 phase. Note that the material is no longer in its pristine perovskite phase after the initial scan and the "c" subscript only serves to illustrate the corresponding plane in the pristine phase. Scale bar, 10 nm [(A) to (D)].

patterns alone (*30*); however, we note that this approach struggles to distinguish between ordered loss of FA^+ and I^-. Although vacancy ordering is clearly apparent on the FA^+ sublattice, there is no equivalent effect evident for the I or Pb/I columns (see fig. S8A for intensity line profiles corresponding to Fig. 3D). Our direct interpretation of real-space images is thus able to reveal that the degradation is strongly driven by the loss, and likely subsequent reordering, of FA^+ ions.

As further elaborated below, these microstructural features help to explain important phenomena pertinent to perovskite solar cells. Specifically, small amounts of PbI_2 are not detrimental to the solar cell performance (*14*–*16*) because perfect crystallographic alignment between the PbI_2 and $FAPbI_3$ perovskite occurs at the material interface, and no crystal defects are apparent in this region. The observation of the checkered pattern further explains why the perovskite structure can sustain substantial deviations from stoichiometry and recover remarkably well from damage.

We note that at cryogenic temperatures, $MAPbI_3$ has been shown to amorphize under electron irradiation rather than inducing the gradual, ordered restructuring of the crystal observed at room temperature (*29*). Rothmann *et al.* argued that such amorphization at low temperatures is the result of impeded ion mobility (*29*), further supporting our notion here that ion migration is a key factor in mitigating the beam-induced damage through atomic rearrangement.

We further examined the nature of the native interfaces formed between $FAPbI_3$ and its precursor PbI_2 (Fig. 3). Small amounts of PbI_2 surprisingly do not impede solar cell performance (*14*–*16*), but the reasons for such benign influence are still a matter of debate. We were able to reveal the presence of a low-misfit, low–lattice strain interface between $FAPbI_3$ and PbI_2 by examining the intergrowth between $FAPbI_3$ and PbI_2 in a film grown specifically under PbI_2-rich conditions (see materials and methods). In Fig. 3B, a nanoscopic domain of PbI_2 with a continuous transition into $FAPbI_3$ can be seen in the upper right corner, with the continuous transition likely arising because of the inclination of the interface to the beam direction. The PbI_2 domain perfectly follows the surrounding perovskite structure and orientation. The lack of evidence for misfit dislocations (see fig. S9 for more examples) shows that the interface is highly coherent and epitaxial. We note that the known 2H hexagonal phase of PbI_2 could not be coherent with the cubic $FAPbI_3$ in all directions in the interface, but that a modified 2H structure described in fig. S10 can be coherent with the perovskite and is possibly stabilized by its interface with $FAPbI_3$ (see fig. S10 for an atomic model), as evidenced by the

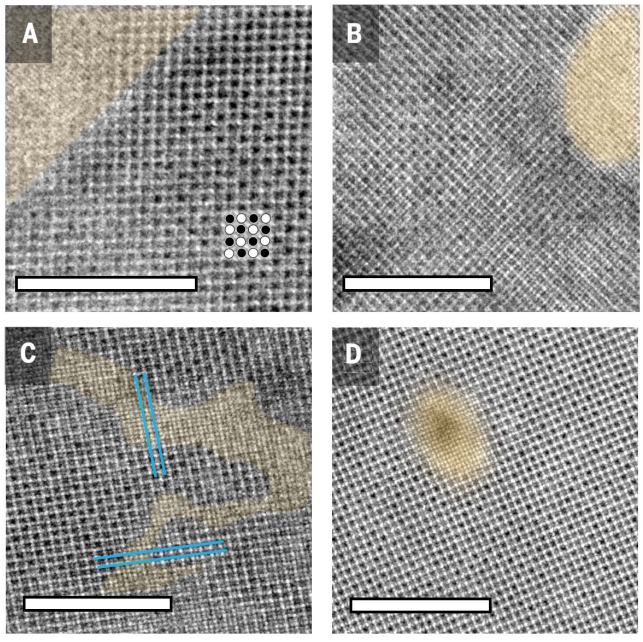

Fig. 3. Atomic-resolution LAADF micrographs of $FAPbI_3$ thin films showing undistorted transitions between PbI_2 and $FAPbI_3$, as well as a checkered intensity after mild radiation damage. PbI_2 is highlighted in light orange. (**A** to **C**) Native intergrowth between PbI_2 and $FAPbI_3$ formed during the deposition process in 90-nm-thick $FAPbI_3$ films fabricated with excess PbI_2. (**D**) A local area of PbI_2 formation induced by focusing an electron beam on a near-stoichiometric $FAPbI_3$ thin film. The highlighted area in (D) corresponds to the damage phase displayed in Fig. 2C; the surrounding area corresponds to that shown in Fig. 2B. The transitions do not induce any measurable phase boundary misfit distortions in the crystal lattice. The nanoscopic PbI_2 domain surrounded by $FAPbI_3$ in (C) indicates that PbI_2 can act as a seed for growth of $FAPbI_3$ crystals. The parallel blue lines in (C) begin in a Pb/I lattice site and end in an FA^+ lattice site after crossing a PbI_2 domain, indicating that areas on either side of the PbI_2 are crystallographically separated and that the presence of PbI_2 is not beam-induced. A checkered pattern in the intensity of the FA^+ lattice site is visible in (A), (C), and (D), schematically shown as black and white circles in (A). This pattern is indicative of a highly ordered restructuring of the moieties in the crystal after mild electron radiation damage. The Fourier transform of (A) is shown in fig. S6. All micrographs were Butterworth-filtered. Scale bars, 10 nm. The same figure is shown without the overlaid color graphics and with Fourier transforms in fig. S7.

square nature of the observed lattice. The weak van der Waals binding between the strongly ionically bound PbI_2 sheets enables the existence of many different PbI_2 polytypes (*44*), and a small shift between the layers of the 2H structure does allow coherent interfaces to form with $FAPbI_3$ (fig. S10) (*44*). This coherence also indicates that the PbI_2 has either acted as a seed for the surrounding perovskite or has grown out of the perovskite because of a local lack of FAI.

Further evidence for PbI_2 seeding is revealed in Fig. 3C, where irregularly shaped domains of PbI_2 can be seen to interweave with the perovskite lattice. Here, we observe a shift of half a unit cell in the perovskite crystal across the PbI_2 domain, as evidenced by the two sets of parallel blue lines. These lines, oriented in the ⟨100⟩ direction, begin in an FA^+ lattice site on one side of the PbI_2 domain and end in a Pb/I lattice site on the other side. These columns are not found together on the same {100} plane in a perfect crystal, so there must be a relative shift of half a unit cell on either side of the PbI_2 region. The LAADF signal intensity line profile displayed in fig. S8B further illustrates this shift across the PbI_2 region. It is unlikely for degradation of $FAPbI_3$ to have resulted in the growth of such an epitaxial PbI_2 phase that exhibits a half-unit cell distortion of the $FAPbI_3$ matrix, because the low misfit of the interface would not give a driving force for such a distortion of the $FAPbI_3$ structure. We can therefore conclude that the perovskite has grown out of the PbI_2 and not vice versa. Despite this shift, geometric phase analysis strain mapping (fig. S11) shows an absence of substantial strain associated with this perovskite/PbI_2 interface. Shown in fig. S12, A and B, are examples of the half-unit cell shift and the PbI_2 intergrowth, respectively, similarly occurring in pristine perovskite that has not suffered electron beam damage. These observations provide further evidence that the presence of perovskite/PbI_2 intergrowth is not caused by radiation-induced damage, but is an intrinsic property of the material, present from the point of crystal growth. To verify that this approach is also applicable to other hybrid perovskites, we also imaged PbI_2-rich $MAPbI_3$ and found similar crystallographic properties (fig. S13).

Grain boundaries and crystal defects

We further revealed the nature of the boundaries between individual $FAPbI_3$ grains through high-resolution LAADF imaging. Such grain boundaries are of particular interest for perovskite solar cells because they have been proposed to act both as charge recombination centers (*18*, *45*, *46*) and as conduction pathways (*16*). In addition, grain boundaries have been shown to be intimately linked with the long-term stability of MHPs such as $FAPbI_3$ (*22*) and the photostability of mixed-halide perovskites toward halide segregation (*23*). Therefore, much effort has been devoted to passivating their negative impact and promoting their positive influence through appropriate treatments and film growth (*11*, *16*, *19*, *47*–*50*). Although many techniques have been used to infer properties of the grain boundaries in photoactive perovskites (*11*, *17*), reliable imaging with atomic resolution has remained elusive, which has led to some uncertainty about the inherent nature of the boundaries (*17*, *50*). A full understanding of the crystallographic nature of grain boundaries is likely to explain a plethora of observations already well established in the field of perovskite solar cell devices, leading to further improvements in performance.

Butterworth-filtered LAADF images (Fig. 4, A to C) illustrate a representative set of grain boundaries in an evaporated thin film of $FAPbI_3$, with several striking features. First, the grains are highly crystalline adjacent to the boundaries, showing that the presence of the boundaries does not disrupt the long-range crystal quality of the surrounding perovskite. Second, the grain boundaries themselves are clearly defined, with the perovskite structure remaining unchanged to the interface, with no obvious preferred interfacial orientation and typically no amorphous material visible. These two points are illustrated by the strain maps displayed in fig. S16. Although an exhaustive description of the strain associated with all the potential boundaries is beyond the scope of this study, we have mapped the strain associated with the low-angle grain boundary seen in the lower left of Fig. 4B. We find that the strain is negligible to within one or two unit cells away from the boundary. Along the boundary itself, the strain exhibits a periodic behavior with alternating sign, which arises from the periodic array of edge dislocations forming the grain boundary. The *yy* strain (lying close to perpendicular to the dislocation Burgers vectors) is much lower at the boundary.

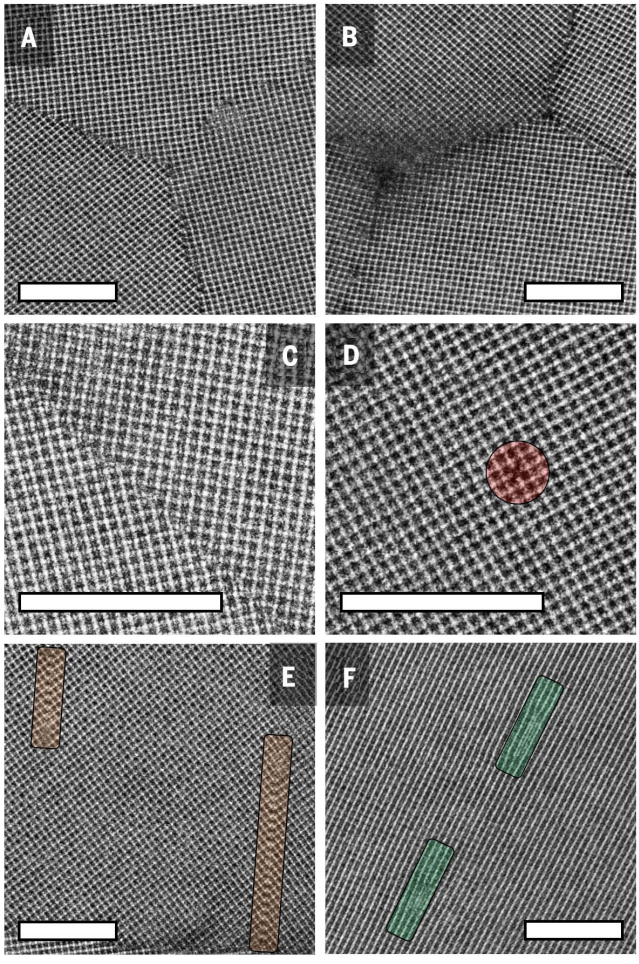

Fig. 4. Butterworth-filtered atomic-resolution LAADF micrographs of representative $FAPbI_3$ grain boundaries and crystal defects as seen in a 30-nm-thick film prepared close to the correct stoichiometry. (**A**) Abrupt grain boundaries meeting at a triple junction showing no amorphous or intergranular phase. (**B**) A triple junction showing signs of amorphization in the intersection at left and a line of vacancies at the intersection at right. The boundaries appear randomly oriented, with the presence of a curved boundary visible in the upper right corner. The low-angle grain boundary at the lower left is formed by a series of ⟨100⟩ edge dislocations. (**C**) A straight section of a grain boundary with virtually no empty lattice sites and very little distortion across the boundary. (**D**) Aligned vacancy defects on the I/Pb lattice site are seen in the red circle. (**E**) Intrinsic stacking faults are seen in the orange rectangles with a stacking fault vector of ½⟨110⟩. (**F**) Edge dislocations are seen in the green rectangles with a Burgers vector of ⟨100⟩. The dislocations can be seen to have dissociated in the climb direction, forming two partial dislocations with Burgers vector ½⟨100⟩ when projected into the image plane, resulting in a fault lying perpendicular to the glide plane. Scale bars, 10 nm. The figure is shown without the colored highlights in fig. S15.

Near-120° triple boundaries are commonly observed at the intersection of three grains. Figure 4A shows a typical image of a triple boundary in a $FAPbI_3$ film, which we generally found to be crystallographically continuous, with minimal lattice distortion and no defects extending away from the grain boundary plane associated with them. Across the STEM micrographs examined, we found this type of "clean" triple boundary to be the most common in $FAPbI_3$, with fig. S14 providing further examples as well as an illustration of the wide range of grain boundary angles found within the films.

Although most grain boundaries in these evaporated $FAPbI_3$ films appear to be highly ordered and sharp, some exceptions also occur. For example, the triple boundary displayed in Fig. 4B contains amorphous material and aligned point defects, as seen at the left and right, respectively. Such variation in the nature of grain boundaries observed here for $FAPbI_3$ may thus also explain the disparity in the grain boundary properties reported in $MAPbI_3$, ranging from detrimental (*18*, *45*, *46*) to beneficial (*16*), or even both (*11*, *17*). If a particular preparation method favors a particularly beneficial or detrimental type of grain boundary, it can improve or decrease solar cell performance, respectively.

Finally, we uncovered the presence of aligned point defects and stacking faults in $FAPbI_3$. The nature and distribution of crystal defects in photoactive perovskites is a topic that has received much attention, but the exact nature of these defects is still unclear (*41*). Most studies and simulations have focused on point defects and their influence on charge-carrier properties (*51*). As revealed in Fig. 4D, aligned point defects in the form of vacancies on the Pb-I sublattice are indeed present in the $FAPbI_3$ crystal. We find here that stacking faults (Fig. 4E) and edge dislocations (Fig. 4F) are also very common in $FAPbI_3$.

Interestingly, the stacking faults shown in Fig. 4E correspond to a shift of half a unit cell, connecting Pb-I columns with I^- columns rather than with Pb-I columns. Edge dislocations are also present, as highlighted in the green rectangles in Fig. 4F. The dislocations are dissociated in a direction perpendicular to their glide plane, and are thus referred to as climb-dissociated, with an apparent region of PbI_2 forming the planar fault that joins the dislocations.

Discussion

Resolving the atomic structure of $FAPbI_3$ thin films allows us to explain many of the intriguing properties of MHPs that had already been well established in the literature but had remained mysterious. The observed loss of FA^+ through an intermediate perovskite structure displaying a checkered FA^+ vacancy pattern provides direct clues to the ability of MHPs to sustain deviations in stoichiometry, and to the regenerative capacity of hybrid organic-inorganic MHPs. This mechanism is likely to be general, given that gradual changes have also been observed in photoluminescence and cathodoluminescence spectra when MHPs are exposed to photon (*52*) and electron (*53*) irradiation, respectively; such changes do not occur in all-inorganic photoactive perovskites (*53*). It can also be presumed to underpin the readily regenerative properties of photobleached $MAPbI_3$ solar cells when they are exposed to gaseous MAI (*13*); such a mechanism would be consistent with the lead iodide perovskite framework remaining even after substantial loss of the organic A-cation. This highly adaptable and resilient structure can thus accommodate large stoichiometry changes without collapsing, which, along with its potential for regeneration, is a clear advantage for applications. Such resilience of structure, induced by ion migration, may well be unique to MHPs, as compared to other more covalent crystalline solids, and is likely to be the origin of the "radiation hardness" of MHPs, which

makes them useful in space applications and as gamma and x-ray detectors.

In addition, the observed atomically coherent nature of perovskite/PbI_2 interfaces explains how the presence of PbI_2 can enhance the crystal quality of MHP films (*16*) by acting as seeds for crystal growth while not adversely affecting the local optoelectronic properties of the material. Higher-energy charge carriers generated in PbI_2 can easily transfer to the lower-energy perovskite, thereby contributing to the overall photogenerated current (*54*), which is relatively unaffected by the perovskite/PbI_2 boundaries. The highly ordered nature of the perovskite/PbI_2 boundary is therefore a core mechanism underpinning the facile fabrication of high-performance solar cells. In essence, this feature forms the MHP analog of the native SiO_2-Si interface, which is benign and is probably the main reason why our electronics industry is primarily based on silicon.

The presence of predominantly sharp, strain-free boundaries between individual $FAPbI_3$ grains is a vital clue to the reasons for the high performance of perovskite solar cells based on polycrystalline films. Grain boundaries in other polycrystalline semiconductor solar cells are generally detrimental to performance, decreasing the short-circuit current density and introducing trap states (*55*, *56*). The revelation of such sharp boundaries in evaporated $FAPbI_3$ films, with some amorphous exceptions, therefore presents a first step toward understanding the exact nature of grain boundaries in perovskite solar cells, through which improved control can ensure the highest possible solar cell performance and stability. In addition, our acquisition of truly atomic-resolution images, enabled through careful choices of image acquisition and filtering approaches, will form the basis of investigations into the microstructure of MHPs across a wide range of different stoichiometries. For example, the addition of small fractions of Cs to replace some of the FA cations in $FAPbI_3$ has been shown to enhance material stability and crystallinity (*57*), which may link with the nature of grain boundaries.

Finally, stacking faults have been shown to act as recombination sites in dislocation-free silicon (*58*), and edge dislocations decrease the photoluminescence intensity in multicrystalline silicon (*59*). Our identification of aligned point defects in the form of vacancies on the FA^+ sublattice and climb-dissociated dislocations in $FAPbI_3$ provides first insights into the specific forms taken by such defects in MHPs. Such information will pave the way for future modeling of defects based on first principles, which can reveal the impact such defects have on the optoelectronic properties of MHPs, and the subsequent performance of perovskite solar cells.

Materials and methods

Sample preparation

$FAPbI_3$ and $MAPbI_3$ thin films were deposited on the carbon-coated side of 300-mesh copper TEM grids. Immediately before deposition, the grids were cleaned with O_2 plasma for 0.3 min. $CH(NH)_2I$ (FAI) and PbI_2 were co-evaporated in a customized thermal evaporation chamber described previously (*60*). Heating of the sources started when the chamber pressure fell below 5×10^{-6} mbar. The PbI_2 rate was kept constant at 0.23 Å s^{-1}, measured using a gold-plated quartz microbalance (QMB). For the "PbI_2-rich" $FAPbI_3$ films with substantial excess of PbI_2, the FAI rate was set to 40% of the rate used for the "near-stoichiometric" $FAPbI_3$ films. This resulted in FAI crucible temperatures of ~150°C during the deposition of the PbI_2-rich $FAPbI_3$ films and 180°C during the deposition of the near-stoichiometric $FAPbI_3$ films. During deposition, the pressure increased to 1×10^{-5} to 2×10^{-5} mbar for the PbI_2-rich $FAPbI_3$ films, and to 5×10^{-5} to 9×10^{-5} mbar for the near-stoichiometric $FAPbI_3$ films. The duration of the overall perovskite deposition was controlled such that the film thickness was 90 nm for the PbI_2-rich $FAPbI_3$ films and 30 nm for the near-stoichiometric $FAPbI_3$ films. After deposition, all films were annealed at 170°C for 1 min. The films were stored in a nitrogen-filled glove box after preparation and transported to the microscope in a triple-sealed nitrogen atmosphere to prevent exposure to moisture.

$CH_3NH_3PbI_3$ ($MAPbI_3$) thin films were prepared using a recently published method (*32*). CH_3NH_3I (MAI, Greatcell) and PbI_2 (99.999% metal base, Sigma-Aldrich) were co-evaporated in the same custom Lesker thermal evaporator chamber. Heating of the sources started when the chamber pressure fell below 5×10^{-6} mbar. During the subsequent evaporation, the pressure increased to 1×10^{-5} to 2×10^{-5} mbar. The PbI_2 rate was kept constant at 0.30 Å s^{-1} using a gold-plated QMB; the MAI temperature was controlled to aim for an overall $MAPbI_3$ deposition rate of 0.45 Å s^{-1}, as measured by a QMB located next to the substrate. For the depositions used in this work, this involved ramping the MAI crucible from 175.1°C to 175.6°C over 1070 s, for 1.1 g of MAI initially in the crucible. The substrate was cooled to 0°C during the deposition; the sensors were cooled to 17°C.

All samples were loaded rapidly into the microscope, being in contact with air for less than 1 min. Perovskite film thicknesses were determined from calibration of material deposition rates of the two sources according to QMB readings inside the vacuum chamber, supported by film depositions on hard transparent quartz substrates for which film thickness readings were determined from a combination of Dektak profilometer readings and optical transmission measurements.

Image acquisition

Microscopy for imaging and condition development was performed on two microscopes. LAADF and HAADF imaging was performed on a JEOL ARM-200F cold FEG, Cs probe–corrected STEM, using 200 kV acceleration voltage and 20 to 21 mrad convergence angle. An annular dark field detector at 8 cm camera length was used for signal acquisition, with inner and outer collection angles of 33 and 120.77 mrad for LAADF imaging, and 72.80 and 235.75 mrad for HAADF imaging, respectively. A JEOL ARM-300F C_s probe–corrected STEM at 300 kV was used for imaging condition development. Both room-temperature and cryogenic conditions were examined, and the cryogenic conditions did not noticeably reduce the beam sensitivity of the $FAPbI_3$ thin films, so all imaging was done at room temperature. Similarly, no noticeable difference in beam sensitivity was found between 200 and 300 kV acceleration voltage, but the material was found to damage faster at 80 kV. All imaging presented in the manuscript was at 200 kV. All alignments and focusing were done away from the areas imaged to reduce electron beam–induced damage to the material. All micrographs were obtained without tilting the sample to reduce the beam damage. The specific image acquisition conditions for all images are listed in table S1.

REFERENCES AND NOTES

1. H.-S. Kim *et al.*, Lead iodide perovskite sensitized all-solid-state submicron thin film mesoscopic solar cell with efficiency exceeding 9%. *Sci. Rep.* **2**, 591 (2012). doi: 10.1038/srep00591; pmid: 22912919
2. M. Liu, M. B. Johnston, H. J. Snaith, Efficient planar heterojunction perovskite solar cells by vapour deposition. *Nature* **501**, 395–398 (2013). doi: 10.1038/nature12509; pmid: 24025775
3. H. Zhou *et al.*, Interface engineering of highly efficient perovskite solar cells. *Science* **345**, 542–546 (2014). doi: 10.1126/science.1254050; pmid: 25082698
4. N. J. Jeon *et al.*, Solvent engineering for high-performance inorganic-organic hybrid perovskite solar cells. *Nat. Mater.* **13**, 897–903 (2014). doi: 10.1038/nmat4014; pmid: 24997740
5. J.-P. Correa-Baena *et al.*, The rapid evolution of highly efficient perovskite solar cells. *Energy Environ. Sci.* **10**, 710–727 (2017). doi: 10.1039/C6EE03397K
6. M. Saliba *et al.*, Incorporation of rubidium cations into perovskite solar cells improves photovoltaic performance. *Science* **354**, 206–209 (2016). doi: 10.1126/science.aah5557; pmid: 27708053
7. D. P. McMeekin *et al.*, A mixed-cation lead mixed-halide perovskite absorber for tandem solar cells. *Science* **351**, 151–155 (2016). doi: 10.1126/science.aad5845; pmid: 26744401
8. D. W. deQuilettes *et al.*, Photo-induced halide redistribution in organic-inorganic perovskite films. *Nat. Commun.* **7**, 11683 (2016). doi: 10.1038/ncomms11683; pmid: 27216703
9. C. C. Stoumpos, C. D. Malliakas, M. G. Kanatzidis, Semiconducting tin and lead iodide perovskites with organic cations: Phase transitions, high mobilities, and near-infrared photoluminescent properties. *Inorg. Chem.* **52**, 9019–9038 (2013). doi: 10.1021/ic401215x; pmid: 23834108
10. T. Baikie *et al.*, A combined single crystal neutron/X-ray diffraction and solid-state nuclear magnetic resonance study of the hybrid perovskites $CH_3NH_3PbX_3$ (X= I, Br and Cl). *J. Mater. Chem. A* **3**, 9298–9307 (2015). doi: 10.1039/C5TA01125F
11. M. U. Rothmann, W. Li, J. Etheridge, Y. B. Cheng, Microstructural Characterisations of Perovskite Solar Cells—From Grains to Interfaces: Techniques, Features, and Challenges. *Adv. Energy Mater.* **7**, 1700912 (2017). doi: 10.1002/aenm.201700912

12. K. Domanski, E. A. Alharbi, A. Hagfeldt, M. Grätzel, W. Tress, Systematic investigation of the impact of operation conditions on the degradation behaviour of perovskite solar cells. *Nat. Energy* **3**, 61–67 (2018). doi: 10.1038/s41560-017-0060-5
13. L. Hong *et al*., Improvement and Regeneration of Perovskite Solar Cells via Methylamine Gas Post-Treatment. *Adv. Funct. Mater.* **27**, 1703060 (2017). doi: 10.1002/adfm.201703060
14. D. H. Cao *et al*., Remnant PbI_2, an unforeseen necessity in high-efficiency hybrid perovskite-based solar cells? *APL Mater.* **2**, 091101 (2014). doi: 10.1063/1.4895038
15. H.-Y. Hsu *et al*., Optimization of PbI_2/$MAPbI_3$ perovskite composites by scanning electrochemical microscopy. *J. Phys. Chem. C* **120**, 19890–19895 (2016). doi: 10.1021/acs.jpcc.6b07850
16. Y. C. Kim *et al*., Beneficial effects of PbI_2 incorporated in organo-lead halide perovskite solar cells. *Adv. Energy Mater.* **6**, 1502104 (2016). doi: 10.1002/aenm.201502104
17. J.-W. Lee *et al*., The role of grain boundaries in perovskite solar cells. *Mater. Today Energy* **7**, 149–160 (2018). doi: 10.1016/j.mtener.2017.07.014
18. R. Long, J. Liu, O. V. Prezhdo, Unravelling the effects of grain boundary and chemical doping on electron–hole recombination in $CH_3NH_3PbI_3$ perovskite by time-domain atomistic simulation. *J. Am. Chem. Soc.* **138**, 3884–3890 (2016). doi: 10.1021/jacs.6b00645; pmid: 26930494
19. T. Niu *et al*., Stable High-Performance Perovskite Solar Cells via Grain Boundary Passivation. *Adv. Mater.* **30**, e1706576 (2018). doi: 10.1002/adma.201706576; pmid: 29527750
20. S. Jariwala *et al*., Local crystal misorientation influences non-radiative recombination in halide perovskites. *Joule* **3**, 3048–3060 (2019). doi: 10.1016/j.joule.2019.09.001
21. C. L. Davies *et al*., Impact of the organic cation on the optoelectronic properties of formamidinium lead triiodide. *J. Phys. Chem. Lett.* **9**, 4502–4511 (2018). doi: 10.1021/acs.jpclett.8b01628; pmid: 30036475
22. S. K. Yadavalli *et al*., Mechanisms of Exceptional Grain Growth and Stability in Formamidinium Lead Triiodide Thin Films for Perovskite Solar Cells. *Acta Mater.* **193**, 10–18 (2020). doi: 10.1016/j.actamat.2020.03.036
23. A. Knight, L. M. Herz, Preventing phase segregation in mixed-halide perovskites: A perspective. *Energy Environ. Sci.* **13**, 2024–2046 (2020). doi: 10.1039/D0EE00788A
24. O. Breitenstein, J. Rakotoniaina, M. H. Al Rifai, M. Werner, Shunt types in crystalline silicon solar cells. *Prog. Photovolt. Res. Appl.* **12**, 529–538 (2004). doi: 10.1002/pip.544
25. A. Stoffers *et al*., Complex Nanotwin Substructure of an Asymmetric Σ9 Tilt Grain Boundary in a Silicon Polycrystal. *Phys. Rev. Lett.* **115**, 235502 (2015). doi: 10.1103/PhysRevLett.115.235502; pmid: 26684123
26. Y. Yu *et al*., Atomic resolution imaging of halide perovskites. *Nano Lett.* **16**, 7530–7535 (2016). doi: 10.1021/acs.nanolett.6b03331; pmid: 27960472
27. D. Zhang *et al*., Atomic-resolution transmission electron microscopy of electron beam-sensitive crystalline materials. *Science* **359**, 675–679 (2018). doi: 10.1126/science.aao0865; pmid: 29348363
28. Y. Li *et al*., Unravelling degradation mechanisms and atomic structure of organic-inorganic halide perovskites by cryo-EM. *Joule* **3**, 2854–2866 (2019). doi: 10.1016/j.joule.2019.08.016
29. M. U. Rothmann *et al*., Structural and chemical changes to $CH_3NH_3PbI_3$ induced by electron and gallium ion beams. *Adv. Mater.* **30**, e1800629 (2018). doi: 10.1002/adma.201800629; pmid: 29700861
30. S. Chen *et al*., Atomic scale insights into structure instability and decomposition pathway of methylammonium lead iodide perovskite. *Nat. Commun.* **9**, 4807 (2018). doi: 10.1038/s41467-018-07177-y; pmid: 30442950
31. R. Hooley, A. Brown, A. Kulak, F. Meldrum, R. Brydson, *J. Phys. Conf. Ser.* **902**, 012005 (2017). doi: 10.1021/acsenergylett.0c00183; pmid: 32296733
32. K. B. Lohmann *et al*., Control over crystal size in vapor deposited metal-halide perovskite films. *ACS Energy Lett.* **5**, 710–717 (2020). doi: 10.1021/acsenergylett.0c00183; pmid: 32296733
33. J. Borchert *et al*., Large-area, highly uniform evaporated formamidinium lead triiodide thin films for solar cells. *ACS Energy Lett.* **2**, 2799–2804 (2017). doi: 10.1021/acsenergylett.7b00967
34. J. Gonnissen *et al*., Optimal experimental design for the detection of light atoms from high-resolution scanning transmission electron microscopy images. *Appl. Phys. Lett.* **105**, 063116 (2014). doi: 10.1063/1.4892884
35. L. Oesinghaus *et al*., Toward tailored film morphologies: The origin of crystal orientation in hybrid perovskite thin films. *Adv. Mater. Interfaces* **3**, 1600403 (2016). doi: 10.1002/admi.201600403
36. H. J. Jung *et al*., Stability of halide perovskite solar cell devices: In situ observation of oxygen diffusion under biasing. *Adv. Mater.* **30**, e1802769 (2018). doi: 10.1002/adma.201802769; pmid: 30133013
37. T. W. Kim *et al*., Self-Organized Superlattice and Phase Coexistence inside Thin Film Organometal Halide Perovskite. *Adv. Mater.* **30**, 1705230 (2018). doi: 10.1002/adma.201705230; pmid: 29318666
38. Z. Chen, Z.-G. Gu, W.-Q. Fu, F. Wang, J. Zhang, A confined fabrication of perovskite quantum dots in oriented MOF thin film. *ACS Appl. Mater. Interfaces* **8**, 28737–28742 (2016). doi: 10.1021/acsami.6b11712; pmid: 27723302
39. M. Xiao *et al*., A fast deposition-crystallization procedure for highly efficient lead iodide perovskite thin-film solar cells. *Angew. Chem.* **126**, 10056–10061 (2014). doi: 10.1002/ange.201405334; pmid: 25047967
40. Y. Zhou, H. Sternlicht, N. P. Padture, Transmission electron microscopy of halide perovskite materials and devices. *Joule* **3**, 641–661 (2019). doi: 10.1016/j.joule.2018.12.011
41. J. Ran *et al*., Electron-Beam-Related Studies of Halide Perovskites: Challenges and Opportunities. *Adv. Energy Mater.* **10**, 1903191 (2020). doi: 10.1002/aenm.201903191
42. R. F. Egerton, Radiation damage to organic and inorganic specimens in the TEM. *Micron* **119**, 72–87 (2019). doi: 10.1016/j.micron.2019.01.005; pmid: 30684768
43. R. F. Egerton, P. Li, M. Malac, Radiation damage in the TEM and SEM. *Micron* **35**, 399–409 (2004). doi: 10.1016/j.micron.2004.02.003; pmid: 15120123
44. P. A. Beckmann, A review of polytypism in lead iodide. *Cryst. Res. Technol.* **45**, 455–460 (2010). doi: 10.1002/crat.201000066
45. H.-S. Duan *et al*., The identification and characterization of defect states in hybrid organic-inorganic perovskite photovoltaics. *Phys. Chem. Chem. Phys.* **17**, 112–116 (2015). doi: 10.1039/C4CP04479G; pmid: 25354141
46. X. Wen *et al*., Defect trapping states and charge carrier recombination in organic–inorganic halide perovskites. *J. Mater. Chem. C* **4**, 793–800 (2016). doi: 10.1039/C5TC03109E
47. D. W. deQuilettes *et al*., Impact of microstructure on local carrier lifetime in perovskite solar cells. *Science* **348**, 683–686 (2015). doi: 10.1126/science.aaa5333; pmid: 25931446
48. Q. Chen *et al*., Controllable self-induced passivation of hybrid lead iodide perovskites toward high performance solar cells. *Nano Lett.* **14**, 4158–4163 (2014). doi: 10.1021/nl501838y; pmid: 24960309
49. Y. Shao, Z. Xiao, C. Bi, Y. Yuan, J. Huang, Origin and elimination of photocurrent hysteresis by fullerene passivation in $CH_3NH_3PbI_3$ planar heterojunction solar cells. *Nat. Commun.* **5**, 5784 (2014). doi: 10.1038/ncomms6784; pmid: 25503258
50. A. F. Castro-Méndez, J. Hidalgo, J. P. Correa-Baena, The role of grain boundaries in perovskite solar cells. *Adv. Energy Mater.* **9**, 1901489 (2019). doi: 10.1002/aenm.201901489
51. J. M. Ball, A. Petrozza, Defects in perovskite-halides and their effects in solar cells. *Nat. Energy* **1**, 16149 (2016). doi: 10.1038/nenergy.2016.149
52. A. Merdasa *et al*., Super-resolution luminescence microspectroscopy reveals the mechanism of photoinduced degradation in $CH_3NH_3PbI_3$ perovskite nanocrystals. *J. Phys. Chem. C* **120**, 10711–10719 (2016). doi: 10.1021/acs.jpcc.6b03512
53. C. Xiao *et al*., Mechanisms of Electron-Beam-Induced Damage in Perovskite Thin Films Revealed by Cathodoluminescence Spectroscopy. *J. Phys. Chem. C* **119**, 26904–26911 (2015). doi: 10.1021/acs.jpcc.5b09698
54. J. B. Patel *et al*., Photocurrent spectroscopy of perovskite solar cells over a wide temperature range from 15 to 350 K. *J. Phys. Chem. Lett.* **9**, 263–268 (2018). doi: 10.1021/acs.jpclett.7b02935; pmid: 29260569
55. J. D. Zook, Effects of grain boundaries in polycrystalline solar cells. *Appl. Phys. Lett.* **37**, 223–226 (1980). doi: 10.1063/1.91832
56. F. Greuter, G. Blatter, Electrical properties of grain boundaries in polycrystalline compound semiconductors. *Semicond. Sci. Technol.* **5**, 111–137 (1990). doi: 10.1088/0268-1242/5/2/001
57. J.-W. Lee *et al*., Formamidinium and Cesium Hybridization for Photo- and Moisture-Stable Perovskite Solar Cell. *Adv. Energy Mater.* **5**, 1501310 (2015). doi: 10.1002/aenm.201501310
58. L. Kimerling, H. Leamy, J. Patel, The electrical properties of stacking faults and precipitates in heat-treated dislocation-free Czochralski silicon. *Appl. Phys. Lett.* **30**, 217–219 (1977). doi: 10.1063/1.89355
59. H. Sugimoto, M. Inoue, M. Tajima, A. Ogura, Y. Ohshita, Analysis of intra-grain defects in multicrystalline silicon wafers by photoluminescence mapping and spectroscopy. *Jpn. J. Appl. Phys.* **45**, L641–L643 (2006). doi: 10.1143/JJAP.45.L641
60. J. Borchert *et al*., Impurity Tracking Enables Enhanced Control and Reproducibility of Hybrid Perovskite Vapor Deposition. *ACS Appl. Mater. Interfaces* **11**, 28851–28857 (2019). doi: 10.1021/acsami.9b07619; pmid: 31314481

ACKNOWLEDGMENTS

We thank the David Cockayne Centre for Electron Microscopy, University of Oxford, for access and support in the use of the JEOL ARM200F instrument (proposal number EP/K040375/1) and additional instrument provision from the Henry Royce Institute (grant reference EP/R010145/1). We also thank Diamond Light Source for access and support in use of the electron Physical Science Imaging Centre (E02, MG21734) that contributed to the results presented here. L.M.H. and M.B.J. thank the Humboldt Foundation for research awards. **Funding:** Supported by the UK Engineering and Physical Sciences Research Council (EPSRC) through grant EP/P033229/1 and through the EPSRC CDT for New and Sustainable Photovoltaics. **Author contributions:** M.U.R. designed and carried out the electron microscope studies and analyzed and interpreted data. J.S.K. participated in the EM studies and provided insights in data interpretation and during editing. J.B. and K.B.L. prepared the samples. C.M.O. and A.A.S. assisted with the EM studies. L.C. performed the multislice simulations. H.J.S. contributed to data analysis and interpretation. M.B.J., P.D.N., and L.M.H. designed the study, interpreted data, and supervised M.U.R., who wrote the manuscript with input from all co-authors. **Competing interests:** H.J.S. is the chief scientific officer and a director of Oxford PV Ltd., a company that is commercializing perovskite photovoltaic technologies. **Data and materials availability:** The datasets and numerical analysis sets described in this manuscript are available for download from the Oxford University Research Archive, under the following DOI: 10.5287/bodleian:pr10GO0gZ.

SUPPLEMENTARY MATERIALS

science.sciencemag.org/content/370/6516/eabb5940/suppl/DC1
Figs. S1 to S16
Table S1
References (*61*–*68*)

5 March 2020; accepted 3 September 2020
10.1126/science.abb5940

Science

Atomic-scale microstructure of metal halide perovskite

Mathias Uller Rothmann, Judy S. Kim, Juliane Borchert, Kilian B. Lohmann, Colum M. O'Leary, Alex A. Sheader, Laura Clark, Henry J. Snaith, Michael B. Johnston, Peter D. Nellist and Laura M. Herz

Science **370** (6516), eabb5940.
DOI: 10.1126/science.abb5940

Structural secrets of hybrid perovskites

The optoelectronic and photovoltaic applications of polycrystalline hybrid metal halide perovskite films are notable because grain boundaries in most materials cause scattering of charge carriers that decreases performance. Electron microscopy studies of these materials have been hindered by their rapid structural degradation under intense electron beams. Rothmann *et al.* now present an atomic crystallographic structure of formamidinium lead triiodide ($FAPbI_3$) polycrystalline thin films obtained by low-electron-dose scanning transmission electron microscopy with advanced image processing. The crystal structure sustains substoichiometry in the A-site cation, has a nearly perfect crystallographic alignment between PbI_2 impurity phases and the $FAPbI_3$ perovskite, and has atomically clean grain boundaries between polycrystalline domains. These features help to explain the films' surprising regenerative ability, their benign grain boundaries where strain and dislocations appear mostly absent, and why excess lead-iodide precursor can be counterintuitively beneficial.

Science, this issue p. eabb5940

Science (print ISSN 0036-8075; online ISSN 1095-9203) is published by the American Association for the Advancement of Science, 1200 New York Avenue NW, Washington, DC 20005. The title *Science* is a registered trademark of AAAS.